

pubs.acs.org/acssensors Article

Inverted Transflection Spectroscopy of Live Cells Using Metallic Grating on Elevated Nanopillars

Aditya Mahalanabish, Steven H. Huang,* and Gennady Shvets*



Cite This: ACS Sens. 2024, 9, 1218-1226



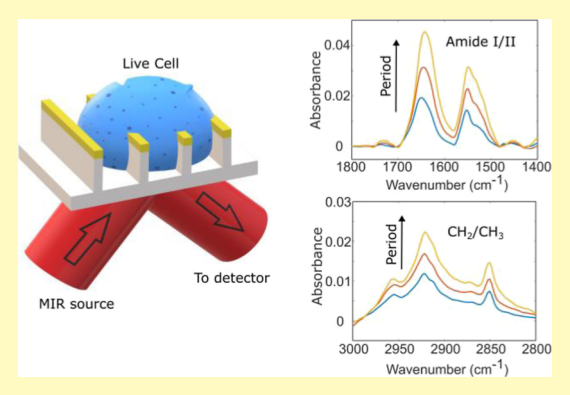
ACCESS I

III Metrics & More

Article Recommendations

Supporting Information

ABSTRACT: Water absorption of mid-infrared (MIR) radiation severely limits the options for vibrational spectroscopy of the analytes—including live biological cells—that must be probed in aqueous environments. While internal reflection elements, such as attenuated total reflection prisms and metasurfaces, partially overcome this limitation, such devices have their own limitations: ATR prisms are difficult to integrate with multiwell cell culture workflows, while metasurfaces suffer from a limited spectral range and small penetration depth into analytes. In this work, we introduce an alternative live cell biosensing platform based on metallic nanogratings fabricated on top of elevated dielectric pillars. For the MIR wavelengths that are significantly longer than the grating period, reflection-based spectroscopy enables broadband sensing of the analytes inside the trenches separating the dielectric pillars. Because the depth of the analyte twice-traversed by the MIR



light excludes the highly absorbing thick water layer above the grating, we refer to the technique as inverted transflection spectroscopy (ITS). The analytic power of ITS is established by measuring a wide range of protein concentrations in solution, with the limit of detection in the single-digit mg mL⁻¹. The ability of ITS to interrogate live cells that naturally wrap themselves around the grating is used to characterize their adhesion kinetic.

KEYWORDS: mid-infrared spectroscopy, transflection, nanopillars, nanogratings, live cells

All-optical label-free sensors have revolutionized the field of analytic life sciences, enabling the detection and quantification of biological objects, such as, proteins, DNA, and live cells. These biosensors have led to significant advances in drug discovery and clinical diagnostics. Mid-infrared (MIR) spectroscopy has emerged as a popular tool for biosensing because of its unique ability to resolve characteristic vibrational fingerprints of the constituent biological molecules. It has already gained significant attention due to its noninvasive, label-free, and rapid detection capabilities. For example, Fourier-Transform Infrared (FTIR) spectroscopy has been used in the past to characterize proteins and polypeptides. ^{1–4}

MIR spectroscopy has also shown great potential in cellular studies. For example, MIR spectroscopy-based cytology, based on the quantification of vibrational fingerprints of cellular molecular constituents (e.g., proteins, lipids, carbohydrates, and nucleic acids), provides an excellent tool for rapid differentiation between different cell types^{5–7} as well as the detection of cellular responses (e.g., apoptosis under cytotoxic conditions) under various influences (e.g., environmental changes, drugs, and other stimuli⁸).

However, MIR spectroscopic measurements suffer from several important limitations that restrict their usefulness for analyzing biological material in aqueous solution, e.g., in patient-derived biofluids, ^{9,10} as well as the FTIR spectroscopy of live cells in their natural environment. The leading issue is

the strong attenuation of mid-IR light in water, which limits the sensitivity of the spectroscopic technique. Because of the water-specific absorption due to the OH bending vibrational band around $\omega_{\rm H-O-H} \sim 1650~{\rm cm}^{-1}$, this issue is particularly severe in the biologically important spectral range 1600 cm⁻¹< ω < 1700 cm⁻¹ associated with Amide I protein vibrations. Measurements using thin microfluidic devices 11,12 and attenuated total reflection-FTIR (ATR-FTIR)¹³⁻¹⁸ have been reported. However, the use of shallow transmission cells (as thin as $6-8 \mu m$) can impose mechanical stress on cells. Water absorption similarly affects another popular approach to collecting the spectra in reflection: the so-called transflectionmode spectroscopy, 19-21 where MIR light passes through the analyte and reflects off a substrate coated with an infraredreflective layer. Using a high-index prism (e.g., diamond) to measure attenuated total reflection (ATR) of MIR light circumvents water absorption 1,17,18,22 and represents a promising approach for broadband spectroscopy. However,

Received: September 26, 2023 Revised: February 4, 2024 Accepted: February 7, 2024 Published: March 12, 2024





diamond ATR can be costly for single-use applications and cannot be easily adapted for high-throughput microwell-based assays²³ that are necessary whenever the number of available cells is limited²⁴ (e.g., when using primary cells). Less expensive microgrooved Si ATR^{25,26} elements could be potentially integrated with standard microwell arrays, but their utility for multispectral imaging applications is limited²⁷ and their submicron penetration depth into a cell¹⁶ can be a drawback whenever cell spectroscopy beyond the plasma membrane and the cytoskeleton is required.

Recently, our group has developed metasurface-enhanced infrared spectroscopy (MEIRS) and used it in a variety of life science applications, including sensing single protein layers,⁴ distinguishing between and capturing of different cell types, 28,29 and, more recently, measuring the MIR spectra of live cells in real time. 30-32 Metasurfaces, made up of arrays of metallic nanoantennas, rely on plasmonic resonances to enhance and localize the optical field around the nanophotonic structures. The coupling of molecular absorption to the plasmonic resonances enables characteristic molecular vibrations to be manifested in the reflected light. By integrating metasurfaces with a traditional FTIR system, our group demonstrated the use of MEIRS as a cellular assay technique to study cell adhesion and detachment, responses of live cells to chemotherapeutics,³² as well as cholesterol depletion from cellular membrane. 30 One drawback of any resonant metasurface is its spectral selectivity; the relatively narrow bandwidth of the resonance can be insufficient for covering the entire fingerprint spectral range. While multiresonant metasurfaces with broad spectral coverage have also been used for biosensing applications, 4,33 such multiresonant metasurfaces still rely on their evanescent fields that cannot penetrate deep into the analyte. While this is not a problem for analytes distributed uniformly across the metasurface, highly heterogeneous samples (e.g., cells) require deeper penetration for sensing those organelles that are not in the immediate proximity (i.e., within about 100 nm²⁸) of the metasurface.

In this work, we propose an alternative concept for a broadband optical device based on nonresonant plasmonic nanostructures (see Figure 1a) that enables measuring MIR spectra of cells and biomolecules in solution. Unlike the MEIRS approach, which is based on resonant metasurfaces, the approach described below does not rely on the localized resonance of plasmonic nanostructures and thus has a much broader spectral sensing range. We refer to the proposed technique as inverted transflection spectroscopy (ITS) because of its similarity to traditional transflection-mode 19–21 measurements, as explained below.

■ THEORETICAL BACKGROUND

ITS measurement is based on the device schematically shown in Figure 1a, comprising an array of gold strips atop silica pillars grown on an IR-transparent substrate. The device functions similarly to a wire grid polarizer under normal incidence, where light with an electric field polarized parallel to the gratings is reflected (with minimal transmission) when the grating periodicity p is much smaller than the incident wavelength $\lambda \equiv 2\pi c/\omega$ of light in vacuum. Analytic expressions for the reflection coefficients $R_{\parallel}^{(gr)}(\omega)$ and $R_{\perp}^{(gr)}(\omega)$ (with incident light polarized parallel and perpendicular to the grating direction, respectively) from a conducting plane with slits are given as follows³⁴

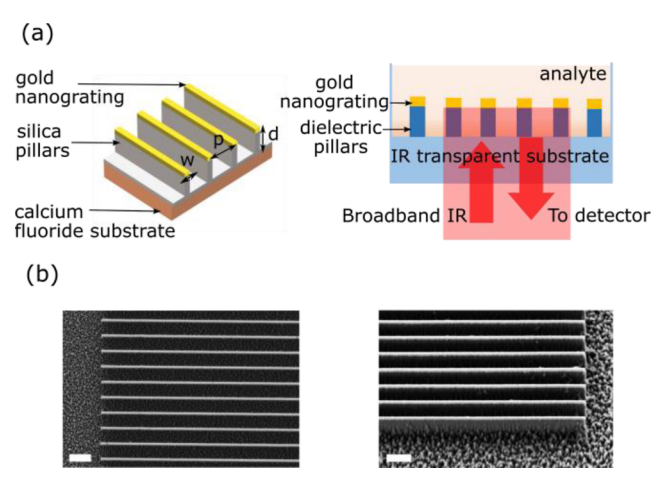


Figure 1. (a) Schematic drawing of the inverted transflection spectroscopy (ITS) device. MIR light polarized along the grating direction and incident from the substrate side reflects from the grating and passes twice through shaded region. (b) SEM images of a fabricated sample. Parameters of the elevated nanograting: w=200 nm, $p=1.35~\mu\text{m}, d=830$ nm. (Left) top view, scale bar: $2~\mu\text{m}$; (Right) same sample viewed at a 35° angle. Scale bar: $1~\mu\text{m}$.

$$R_{\parallel}^{(gr)} = \frac{1}{1 + k^2 p^2 \log^2 \left[\sin \left(\frac{\pi w}{2p} \right) \right] / \pi^2}$$

$$R_{\perp}^{(gr)} = \frac{k^2 p^2 \log^2 \left[\cos \left(\frac{\pi w}{2p} \right) \right] / \pi^2}{1 + k^2 p^2 \log^2 \left[\cos \left(\frac{\pi w}{2p} \right) \right] / \pi^2}$$
(1)

where $k = 2\pi n_{\text{eff}}/\lambda$ is the wavenumber of the incident wave in the embedding medium with a refractive index n_{eff} and w is the width of each conducting strip. Geometric parameters of the elevated nanograting are defined in the left panel of Figure 1a.

It follows from eq 1 that in the long-wavelength limit (defined as $kp \ll 1$), $R_{\parallel}^{(\mathrm{gr})} \approx 1$ and $R_{\parallel}^{(\mathrm{gr})} \approx 0$. The regions of the trenches separating the nanopillars with height d are twice-traversed by the \parallel -polarized component of the incident light. Therefore, the total measured reflectance $R_{\parallel}(\omega)$ accounts for the light absorption inside the analyte layer, whose effective volume is controlled by the geometry of the elevated nanograting.

In contrast to conventional transflection-mode measurements, where the incident light beam traverses the entire analyte (i.e., incident from the top in Figure 1a), the measurement mode considered here corresponds to the light beam incident from the inverted direction, hence, the ITS designation. On the other hand, the \perp -polarized component of the incident beam propagates past the elevated nanograting without reflections and is subsequently absorbed by water.

Therefore, by limiting the sampled region to a small but finite depth d, the inverted geometry enables a transflection-mode measurement that would be impossible to carry out from the opposite direction because of the strong water absorption of MIR light.

Crucially, any analyte contained within the trenches—up to the distance d above the substrate—can be analyzed through ITS by measuring the reflectance $R_{\parallel}(\omega)$, which is a function of $R_{\parallel}^{(gr)}(\omega)$ and absorbance of the analyte. Consequently, the total measured reflectance $R_{\parallel}(\omega)$ depends on (a) the properties of

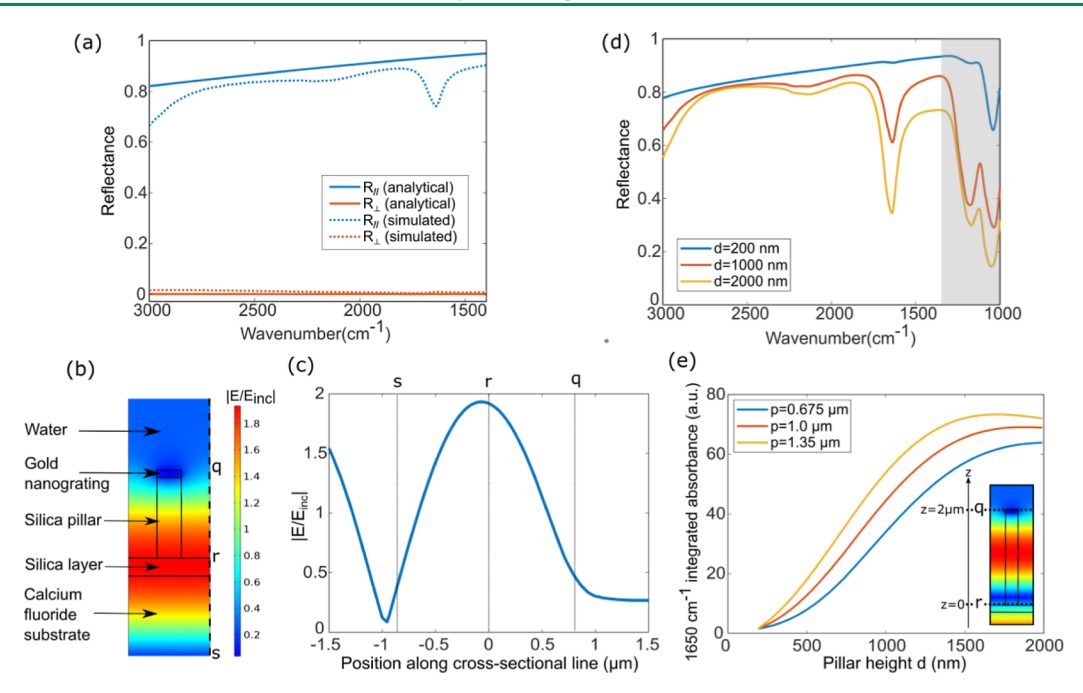


Figure 2. Simulations of ITS for pure water as analyte. (a) Analytic grating reflectance $(R_{\parallel \perp}^{(gr)})$ and simulated total $(R_{\parallel \perp})$ reflectance from the water-filled ITS device. Light is normally incident through the CaF₂ substrate with two polarizations: \parallel or \perp to the grating. (b) Normalized field intensity for \parallel - polarized light with $\lambda = 5 \mu m$. (c) Field intensity along the dotted line marked in (b). Cross section planes q (top of grating), r (silica/analyte interface: z = 0), and s are marked in (b,c). (d) ITS spectra for 3 pillar heights: d = 200, 1000, and 2000 nm; with the grayed-out region marking the silica absorbance bands. (e) Variation of water absorbance at $ω_{H-O-H} \approx 1650$ cm⁻¹, as seen from the ITS spectra, for pillar heights 200 nm < d < 2000 nm. Blue, red, and yellow curves: $p = 0.675 \mu m$, $p = 1.0 \mu m$, and $p = 1.35 \mu m$ periodicities [corresponding to (a–c)], respectively. Inset in (e): same as in (b), but $d = 2 \mu m$. Grating width w = 200 nm for all panels, grating period $p = 0.675 \mu m$ for (a–d), grating height d = 830 nm for (a–c).

the analyte and (b) the optical path length $l \approx 2d$ through the sampled layer (which includes the silica pillars and the analyte) controlled by the height d of the silica pillars. In particular, attenuation of the MIR light in water can be limited to a few micrometers by keeping the pillar height small, making the proposed structure a useful device for measuring aqueous samples as well as live cells in culture medium.

Example: Water-Filled ITS Device. To illustrate the workings of the ITS approach, we begin by examining the simplest case of pure water as an analyte. Analytic calculations (see eq 1) of $R_{\perp}^{(gr)}(\omega)$ and numerical simulations (using COMSOL Multiphysics commercial software package) of $R_{\text{l.l.}}^{(gr)}(\omega)$ were carried out for the following parameters of the elevated grating: p = 675 nm, w = 200 nm, and the grating height d = 830 nm. For the analytic calculations (solid lines in Figure 2a), we chose $n_{\rm eff} = 1.3$ as the frequency-independent average refractive index of water and silica. On the other hand, frequency-dependent tabulated refractive indexes of water and silica are used for the COMSOL simulations exhibited as dashed lines in Figure 2a. The considered spectral range of $1350 \text{ cm}^{-1} < \omega < 3000 \text{ cm}^{-1} \text{ contains several important}$ biological MIR fingerprints. Specifically, the CH₂/CH₃ stretching modes in the 2800-3000 cm⁻¹ region are attributed to lipids,³⁵ amide features in the 1500-1700 cm⁻¹ region are attributed to a combination of C=O stretching, N-H bending, and C-N stretching in the amide backbone of proteins,³⁶ and several smaller features are attributed to phosphates (~1240 cm⁻¹; not examined here) and carbohydrates (1000–1500 cm⁻¹).³⁷ For the \perp -polarized incident light, we observe that $R_{\perp}(\omega) \approx 0$ for all frequencies, as expected because $R_{\perp}^{(gr)}(\omega) \approx 0$. For the \parallel -polarized light, $R_{\parallel}(\omega) \approx R_{\parallel}^{(gr)}(\omega)$ for most frequencies, except for the spectral

region in the vicinity of $\omega \sim \omega_{\text{H-O-H}}$, where water is strongly absorbing. Deviations of R_{\parallel} from $R_{\parallel}^{\text{(gr)}}$ are attributed to transflection-mode absorbance $A(\omega)$: the \parallel -polarized MIR light travels through the silica pillar/analyte layer, reflects from gold, and travels back through the silica pillar/analyte layer for a second time, before being collected at the detector.

Interpreting the resulting transflection spectra $R_{\parallel}(\omega)$ requires considering several effects specific to ITS. First, because the analyte is in the form of a thin film $(d < \lambda)$, there is an electric field standing wave (EFSW)38-40 formed within the analyte layer. This EFSW effect causes the absorbance to change nonlinearly with respect to the sample thickness. Therefore, the Beer-Lambert law, which predicts a linear relationship between absorbance and the analyte depth d, no longer holds because the grating structure produces a complex wave intensity pattern inside the analyte/silica pillar layer. The resultant intensity distribution produced by the interference between the incident and reflected waves from the grating is shown in Figure 2b,c, with Figure 2c showing the electric field intensity variation along the dotted line at the edge of the unit cell. The electric field intensity above the grating remains relatively constant and low due to minimal transmission, whereas below the grating it exhibits an interference pattern.

To gain a comprehensive understanding of the height dependence of the absorbance, we simulated the dependence of the reflectance and absorbance spectra on the pillar height d using water as a model analyte inside the ITS device. Figure 2d illustrates the typical reflectance spectra for the devices with three different pillar heights, d=200, 1000, and 2000 nm. The water absorption line at $\omega_{\rm H-O-H}$ is prominent in the reflectance spectra. The corresponding reflectance dip increases in intensity as the silica pillar height increases, and

ACS Sensors pubs.acs.org/acssensors Article

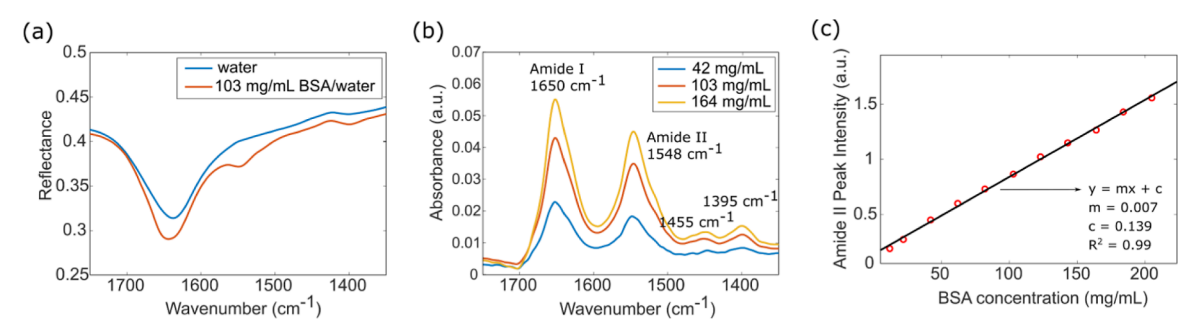


Figure 3. Experimentally measured bovine serum albumin (BSA) spectra were obtained using ITS. (a) Reflectance spectra measured from the nanograting with water and 103 mg/mL BSA solution. (b) Absorbance spectra of BSA in water with concentrations 42, 103, and 164 mg/mL showing several protein-related vibrational peaks. (c) Variation of the integrated peak intensity of the Amide II peak with BSA solution concentration. Nanograting parameters (see Figure 1a for geometry definitions): $p = 0.675 \mu m$, d = 830 nm, and w = 200 nm.

consequently, the sampled analyte thickness is increased. The dependence of the dip magnitude is plotted in Figure 2e as a function of d. The $\sin^2(z)$ dependence of the field intensity resulting from the standing wave pattern gives rise to a nonlinear dependence of the absorbance intensity with the pillar height, as observed in Figure 2e.

Dependence of reflectance and absorbance on device period was also studied (details in Section S3). In short, we observed almost a constant reflectance over the operating range for device periodicity of $p = 0.675 \mu m$ (as in Figure 2a).

However, for increasing periodicities, we observe a sharp drop in reflectance, moving from longer to shorter wavelengths, as is also observed in the experimental measurements shown later. Absorbance scales with period, similar to what is observed in cellular measurements later, due to an increase in analyte volume being sensed.

Taken together, these findings reinforce our interpretation of the reflectance spectrum of unpolarized light, $R(\omega) \approx R_{\parallel}/2$, as the inverse transflectance. In the rest of this work, we experimentally investigate how the inverse transflection absorbance spectra $A(\omega) = -\log_{10}(R_{\rm s}/R_{\rm bg})$ (referred to as absorbance for brevity) can be used for sensing more complex analytes: proteins and live cells in aqueous environment. Here $R_{\rm s}(\omega)$ and $R_{\rm bg}(\omega)$ are the ITS measurements from the analyte-filled (sample) and water-filled (background) structures, respectively. The terms reflectance and transflectance will be used interchangeably in what follows because the former refers to the experimental technique while the latter refers to the physical interpretation of the results.

An important factor limiting the available spectral range of the present implementation of the ITS device to $\omega > 1400$ cm⁻¹ is the presence of silica lattice vibration modes⁴¹ in the $1000~\rm cm^{-1} < \omega < 1350~\rm cm^{-1}$ range gray-shaded in Figure 2d. These reflectance dips are caused by the silica dielectric pillars underneath the gold gratings as well as a thin layer of silica (~200 nm) on the CaF₂ substrate. The reduced raw (unnormalized) transflectance signal in the silica absorption band makes it essentially unusable for quantifying analyte-related spectral features. Therefore, in the rest of the article, this spectral region is excluded from all spectra.

RESULTS AND DISCUSSION

The proposed device was fabricated through plasma-enhanced chemical vapor deposition, electron beam lithography, electron beam evaporation of metals, and reactive ion etching (see the Materials and Methods Section in the Supporting Information). The samples used in this work comprise thin gold

gratings with a width of w = 200 nm atop silica pillars with a height of $d \approx 830$ nm, separated from each other by trenches with a width of t = p - w; see Figure 1b for a SEM image of a typical ITS device. Samples with three grating periodicities ($p = 0.675 \mu m$, 1 μm , and 1.35 μm) were used.

ITS of Protein Solutions. The ITS measurements of aqueous solutions of bovine serum albumin (BSA) of various concentrations were carried out, with the liquid samples completely filling the trench spaces as well as the space above the gratings. Using unpolarized MIR light incident from the CaF₂ side, we carried out the ITS measurements using a device with $p = 1.0 \mu m$. The transflectance spectra for the background (water only; blue line) and the 103 mg/mL BSA/water sample (red line) are plotted in Figure 3a, with the corresponding calculated absorbance shown in Figure 3b as an orange line. The signature MIR spectral peaks of BSA $^{42-44}$ are clearly visible, including the strongest amide I ($\omega_{\text{A-I}} \sim 1650 \text{ cm}^{-1}$) and amide II ($\omega_{\text{A-II}} \sim 1548 \text{ cm}^{-1}$) bands, as well as several weaker ones (C=O stretch in COO around 1,395⁻¹ and CH₂ scissoring around 1455 cm⁻¹). Absorbance spectra for lower (42 mg/mL) and higher (164 mg/mL) BSA concentrations are shown in Figure 3b for comparison. The plot of the amide II peak integrated intensity shown in Figure 3c exhibits a linear dependence on the BSA concentration in accordance with the Beer-Lambert Law. The results of our measurements using ITS devices filled with BSA water solutions demonstrate their utility for MIR spectroscopy of complex liquid analytes, with the measurement setup reminiscent of ATR-FTIR spectroscopy. Figure S1 compares spectra from a 103 mg/mL BSA/water sample obtained using the ITS device and ATR-FTIR. The nanograting device at 830 nm height is approximately 3.5 times less sensitive than the commercial ATR-FTIR used. However, increasing groove depth to around 2 μ m should enhance the sensitivity about 3 times (as can be inferred from the blue curve in Figure 2e), aligning it with ATR-FTIR levels. When using nanogratings with higher periodicities p, the sensitivity can be further increased as evident from the red and yellow curves in Figure 2e. The obtained single-digit mg mL⁻¹ LOD (see section S4) is comparable to that obtained using microstructured Si ATR.45

ITS of Live Cells: General Considerations. Next, we demonstrate that ITS nanogratings can be applied to the MIR spectroscopy of live cells. Compared with those for an aqueous solution of proteins, IR spectra of cells are more complex to measure and interpret because of the heterogeneous distribution of different biomolecules within each cell as well as their fairly complex (and frequently poorly understood)

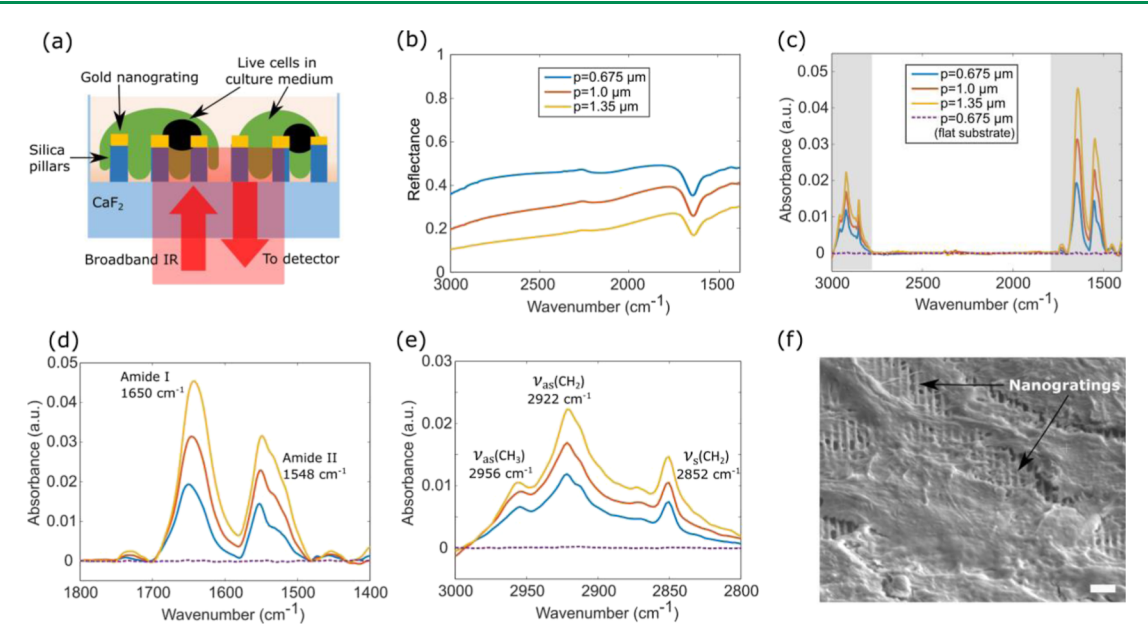


Figure 4. IR spectroscopy of live cells using the ITS device. (a) Schematic of the measurement setup used for cell characterization. (b) Inverted transflectance and (c) corresponding absorbance spectra of A431 cells grown on elevated gratings with 3 grating periodicities (blue: $p = 0.675 \mu m$, red: $p = 1.0 \mu m$, yellow: $d = 1.35 \mu m$; d = 830 nm height for all three) and flat substrate (dotted purple: $p = 0.675 \mu m$). (d,e) Zoomed-in absorbance spectra corresponding to the spectral regions gray-shaded in (c) attributed to (d) proteins (amide I and II) and (e) lipids (CH₂/CH₃), respectively. Dashed purple line: metallic gratings with the period $p = 0.675 \mu m$ and height $d \sim 75.0$ nm are atop the flat silica substrate (no silica pillars). (f) SEM image of fixed-and-dried cells grown on the nanograting ($p = 0.675 \mu m$). Scale bar: $2 \mu m$.

morphology. For example, it is not clear a priori whether a cell can be sufficiently deformed to penetrate into the trenches between the silica pillars. As Figure 2b illustrates, the very success of the nanograting-based ITS depends on such deformations because they ensure sufficient overlap with the MIR optical field inside the trenches.

Cellular interactions with nanotopographies have recently received considerable attention because of the potential effects of three-dimensional (3D) nanostructures on cell adhesion and morphology, 46,47 penetration of cell membrane for cargo delivery, 48 electroporation of the cellular membrane, 49,50 as well as modulation of cell membrane curvatures. 51–54

Crucially, it has been recently reported that, with the appropriate width and periodicity of the nanostructures, many mammalian cell types can deform and tightly wrap around the vertical structures by closely following the nanotopography of the surface. 51-54 The process driving the bending of the cell plasma membrane around such raised nanostructures is clathrin-mediated endocytosis (CME)—the same process by which cells regulate distribution of membrane proteins and entry of extra-cellular species and is one of the primary modes of endocytosis consistently active in all mammalian cells.^{55–57} Moreover, critical cell functions, such as adhesion and membrane integrity, have been shown not to be impaired by the tight wrapping of the cellular membrane around 3D nanostructures.⁵⁸ In particular, interaction of adherent cells with micrometer- and nanometer-scale grooves and ridgessimilar to the ones depicted in Figure 1 but without metallic strips on top-has been studied even earlier for a variety of cell lines. 59-62 The major effect reported for the growth of most cells on such substrates is "contact guidance"—where the cells tend to align and grow along the direction of the grooves, often with the organization of actin filaments and focal adhesions along the same direction. 60,63,64 Although most cell types

exhibit this alignment, certain cells like keratinocytes or neutrophils show no such morphological behavior. ⁶⁵

Nanostructured substrates have long been recognized as distinct cell culture dishes—and have been recently described as "biological metamaterials"66—because of the effect of the topography on cellular attachment, division, and proliferation.⁶⁷ High-aspect silicon-based nanopillars have also been used for enhancing the capture rate of rare cells owing to the local topographic interactions between the nanostructured substrates and nanoscale components of the cellular surface. 68,69 The established fact of numerous cell types adhering closely to nanostructures by wrapping themselves closely around each 3D (elevated) grating structure leads us to surmise that the cells can completely take up the space inside the trenches, thus overlapping with the probing MIR light. Therefore, the effect of the cells lowering themselves into the trenches could be measured by the ITS device as a function of time.

For the A431 (epidermoid carcinoma) cell line used in this work, we have used confocal fluorescence microscopy to confirm that the cells cultured on the fabricated ITS samples indeed envelope the nanopillars and dip into the nanotrenches by deforming their plasma membrane: see Section S5 for additional details.

ITS of Live Cells: End Point Measurements. Because the cells extending into the trenches can be interrogated using ITS, we proceeded to characterize the MIR spectra of live cells cultured atop the nanogratings using FTIR spectroscopy; see Figure 4a for the measurement setup. Specifically, live cells were cultured inside microwells covered underneath by nanograting-containing CaF_2 substrates. The cells were probed from the CaF_2 (bottom) side while they were immersed in a cell culture medium. The measured reflectance spectra, under normally incident unpolarized light, are shown in Figure 4b for cells grown on nanogratings with 3 different periodicities: p =

ACS Sensors pubs.acs.org/acssensors Article

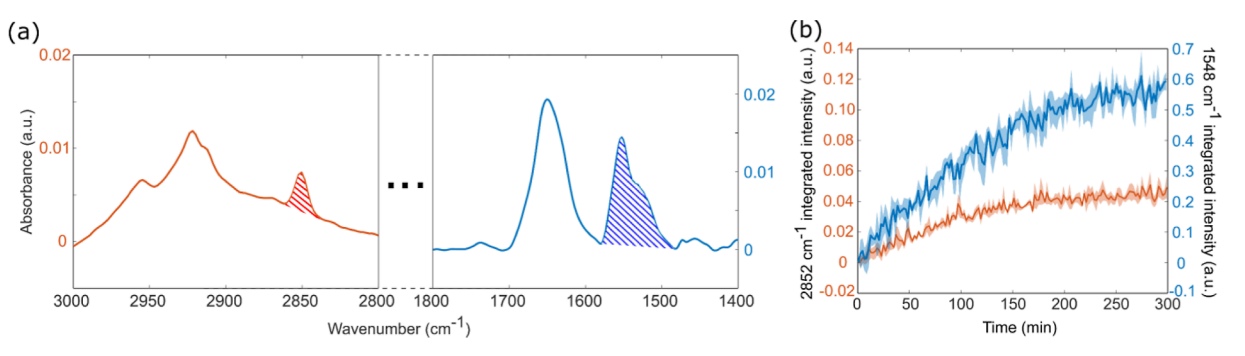


Figure 5. Time evolution of live A431 cell adhesion on the ITS device. (a) Absorbance spectra corresponding to protein (right) and lipid (left) bands, measured using grating with periodicity $p=0.675~\mu\text{m}$, height d=830~nm, and width w=200~nm. Shaded regions indicate the regions over which the peaks were integrated. (b) Time evolution of the integrated peak intensity of amide II band (blue), representing protein signal evolution with cellular adhesion and time evolution of the integrated peak intensity of CH₂ symmetric stretching (red), representing lipid signal evolution with cellular adhesion.

0.675, 1.0, and 1.35 μ m. We observe that, except around the water absorption peak at $\omega_{\rm H-O-H} \sim 1650~{\rm cm}^{-1}$, the grating with $p=0.675~\mu{\rm m}$ consistently provides reflectance in the 0.38 $< R(\omega) < 0.47$ range across the entire measured wavenumber range 1300 cm⁻¹ $< \omega < 3000~{\rm cm}^{-1}$. However, the reflectance steadily decreases with increasing wavenumbers ω for the gratings with p=1.0 or 1.35 μ m. Consistently with eq 1, this observation is attributed to the increased transmission of the grating-polarized light at shorter wavelengths.

On the other hand, increasing the periodicity while keeping the grating width w fixed increases the fractional volume of cells $v_{\rm cell} \sim t/p = 1 - w/p$ in the trenches, resulting in their larger overlap with the optical field and stronger absorbance. Therefore, the optimal periodicity for broadband reflectance measurement requires a balance between maintaining sufficiently high reflectance (i.e., small p) and large $v_{\rm cell}$ (i.e., large trench width t).

Figure 4c shows the calculated cellular absorbance, $A_{\text{cell}}(\omega)$. The close-ups for the regions of interest (protein and lipid bands) plotted in Figure 4d,e provide a clear representation of the cellular vibrational spectra. They are very similar to the absorbance spectra measured in typical FTIR measurements of cells, including in the transmission and ATR-FTIR configurations, as well as our previous metasurface-based measurement using MEIRS. 1,15,29,70,71 Here, the absorbance for the cellular measurements is defined as $A_{\text{cell}}(\omega) = -\log_{10}(R(\omega)^{\text{cell}}/$ $R(\omega)^{\text{med}}$), where $R(\omega)^{\text{cell}}$ and $R(\omega)^{\text{med}}$ are the transflectance spectra measured from the nanograting with live cells in culture medium and from the cell-free culture medium, respectively. The dominant features observed in the cellular absorbance spectra include amide I ($\omega_{A-I} \sim 1650 \text{ cm}^{-1}$) and amide II ($\omega_{A-II} \sim 1548 \text{ cm}^{-1}$) peaks attributable to proteins, as well as the CH₂ symmetric stretching ($\omega_{\rm CH_2}^{(\rm s)}\sim 2852~{\rm cm}^{-1}$), ${
m CH_2}$ antisymmetric stretching ($\omega^{(as)}_{
m CH_2}\sim 2922~{
m cm}^{-1}$), and ${
m CH_3}$ antisymmetric stretching ($\omega_{\rm CH_3}^{\rm (as)} \sim 2852~{\rm cm}^{-1}$) attributed to lipids. We note that while we have chosen to use the reflectance $R(\omega)^{\text{med}}$ from a medium-filled ITS device as a background signal, using water-filled structures as the background would also be acceptable because we did not detect any of the four characteristic frequencies (amides or CH stretches) in $R(\omega)^{\text{med}}$ (not shown). Figure 4f shows the SEM image of fixed and dried A431 cells grown on the ITS sample.

ITS of Live Cells: Real-Time Measurements of Cell Adhesion. To demonstrate the utility of the ITS device for long-term kinetic measurement of live cells, we spectroscopi-

cally characterize cellular adhesion as a function of time using a nanograting with the periodicity $p=0.675~\mu\mathrm{m}$. The reflectance spectra were measured every 2 min for 5 h as the cells were seeded and adhered to the nanograting structures. To observe the evolution in protein and lipid absorbance signals over time, we analyzed the integrated peak intensity of the Amide II peak at $\omega_{\text{A-II}}$ (shaded in Figure 5a right) and the CH₂ symmetric stretching mode at $\omega_{\text{CH}_2}^{(s)}$ (shaded in Figure 5a left), respectively. These intensities were plotted as a function of time in Figure 5b. Our analysis reveals similar trends in the temporal signal evolution for both peaks. Specifically, the signals grow rapidly during the first 140 min, and then their growth rate slows down—consistent with our previous observations of cell adhesion using a plasmonic metasurface. ³¹

Future studies will be extended to investigating whether different surface coatings affect cellular adhesion and growth rate on such nanocontoured substrates. Typically, cell adhesion on flat surfaces is heavily reliant on the presence of extracellular matrix (ECM) adhesion proteins, such as collagen and fibronectin, for integrin-mediated cell adhesion. However, on nanostructured surfaces, it has been reported that clathrin endocytosis complexes forming around the surface protrusions play an important role in cellular interaction with nanostructured surfaces. Specifically, clathrin-mediated endocytosis has been implicated in the formation of membrane curvature around nanostructures.⁵¹ By examining the effects of various surface coatings on cellular adhesion and proliferation rates, we can gain insights into how surface topography influences cell behavior (e.g., by modulating cell membrane curvatures^{51–54}) and potentially develop strategies for enhancing or inhibiting cell adhesion and growth on nanocontoured substrates.

CONCLUSIONS

In this work, we introduced a novel MIR spectroscopy-based live cell biosensing platform—inverted transflection spectroscopy—based on elevated nanogratings. We show that ITS devices produce broadband signals and enable MIR spectroscopy in the 1400—3000 cm⁻¹ spectral range. ITS can be used to characterize analytes in solution or liquid form, as we demonstrate through the IR spectroscopy of BSA solutions. Further, adherent cells can be measured as well, taking advantage of the fact that the cells can deform around the elevated nanogratings and extend into the trenches below. We demonstrated this by characterizing the adhesion kinetics of the live A431 cells through MIR spectroscopy.

ACS Sensors pubs.acs.org/acssensors Article

Currently, the spectral range of the presented ITS device is limited by the absorption caused by the silica layer. To extend the useful spectral range below 1400 cm $^{-1}$, alternative materials such as ${\rm Al_2O_3}$ (see Figure S7), which are more transparent in the relevant spectral region, could be used to fabricate the dielectric pillars. Additionally, the silica pillar height was limited to <1 $\mu{\rm m}$ because of several quality issues we encountered with thicker films. Upon optimization of the plasma-enhanced chemical vapor deposition (PECVD) process, it will be possible to fabricate higher performance ITS devices (see section S2) with pillar heights $d\sim 2~\mu{\rm m}$.

The nanograting-based device described here is somewhat similar to the metasurface-based device reported by our group previously, 30,31 but these two devices have different sensing volumes and can be complementary to each other. Since the metasurface-sensing volume is limited by the near-field decay of the plasmonic hotspots (roughly 100 nm), it is limited to the sensing of the cellular membrane and cellular structures around the membrane. On the other hand, the ITS device described in this work is based on transflectance measurement. As long as the cells can extend into the trenches below the nanograting, they can be probed beyond the cell membrane. Cells can also undergo significant deformation of their nucleus around such vertical nanostructures. 49,72 Such nuclear deformation would enable MIR spectroscopy of the nucleus, an important measurement that will be carried out in our future work. For non-adherent cells, the ITS device can in turn be used to monitor secretion of cell metabolites and uptake of nutrients.

ASSOCIATED CONTENT

Supporting Information

The Supporting Information is available free of charge at https://pubs.acs.org/doi/10.1021/acssensors.3c02031.

Additional simulations and measurements along with information on materials and methods of experiments and simulations performed (PDF)

AUTHOR INFORMATION

Corresponding Authors

Steven H. Huang — School of Applied and Engineering Physics, Cornell University, Ithaca, New York 14853, United States; Email: hh623@cornell.edu

Gennady Shvets — School of Applied and Engineering Physics, Cornell University, Ithaca, New York 14853, United States; Email: gshvets@cornell.edu

Author

Aditya Mahalanabish — School of Applied and Engineering Physics, Cornell University, Ithaca, New York 14853, United States; orcid.org/0000-0002-9489-4863

Complete contact information is available at: https://pubs.acs.org/10.1021/acssensors.3c02031

Author Contributions

The manuscript was written through contributions of all authors. All authors have given approval to the final version of the manuscript.

Notes

The authors declare no competing financial interest. This article was published as a preprint at the following DOI: https://doi.org/10.1101/2023.09.19.558443.

ACKNOWLEDGMENTS

The research reported here was supported by the National Cancer Institute of the National Institutes of Health under award number R21CA251052 and by the National Institute of General Medical Sciences of the National Institutes of Health under award number R21GM138947. This work was performed in part at the Cornell NanoScale Science and Technology Facility (CNF), a member of the National Nanotechnology Coordinated Infrastructure (NNCI), which is supported by the National Science Foundation (Grant NNCI-2025233). This work was also performed in part at the BRC Imaging Facility at Cornell, which is supported by the National Institute of Health (Grant NIH S10RR025502). The authors acknowledge the use of facilities and instrumentation supported by NSF through the Cornell University Materials Research Science and Engineering Center DMR-1719875.

REFERENCES

- (1) Baker, M. J.; Trevisan, J.; Bassan, P.; Bhargava, R.; Butler, H. J.; Dorling, K. M.; Fielden, P. R.; Fogarty, S. W.; Fullwood, N. J.; Heys, K. A.; Hughes, C.; Lasch, P.; Martin-Hirsch, P. L.; Obinaju, B.; Sockalingum, G. D.; Sulé-Suso, J.; Strong, R. J.; Walsh, M. J.; Wood, B. R.; Gardner, P.; Martin, F. L. Using Fourier Transform IR Spectroscopy to Analyze Biological Materials. *Nat. Protoc.* **2014**, 9 (8), 1771–1791.
- (2) Jackson, M.; Mantsch, H. H. The Use and Misuse of FTIR Spectroscopy in the Determination of Protein Structure. *Crit. Rev. Biochem. Mol. Biol.* **1995**, 30 (2), 95–120.
- (3) Yang, H.; Yang, S.; Kong, J.; Dong, A.; Yu, S. Obtaining Information about Protein Secondary Structures in Aqueous Solution Using Fourier Transform IR Spectroscopy. *Nat. Protoc.* **2015**, *10* (3), 382–396.
- (4) Wu, C.; Khanikaev, A. B.; Adato, R.; Arju, N.; Yanik, A. A.; Altug, H.; Shvets, G. Fano-Resonant Asymmetric Metamaterials for Ultrasensitive Spectroscopy and Identification of Molecular Monolayers. *Nat. Mater.* **2012**, *11* (1), 69–75.
- (5) Mordechai, S.; Sahu, R. K.; Hammody, Z.; Mark, S.; Kantarovich, K.; Guterman, H.; Podshyvalov, A.; Goldstein, J.; Argov, S. Possible Common Biomarkers from FTIR Microspectroscopy of Cervical Cancer and Melanoma. *J. Microsc.* **2004**, *215* (1), 86–91.
- (6) Argov, S.; Ramesh, J.; Salman, A.; Sinelnikov, I.; Goldstein, J.; Guterman, H.; Mordechai, S. Diagnostic potential of Fourier-transform infrared microspectroscopy and advanced computational methods in colon cancer patients. *J. Biomed. Opt.* **2002**, *7* (2), 248.
- (7) Diem, M.; Miljković, M.; Bird, B.; Chernenko, T.; Schubert, J.; Marcsisin, E.; Mazur, A.; Kingston, E.; Zuser, E.; Papamarkakis, K.; Laver, N. Applications of Infrared and Raman Microspectroscopy of Cells and Tissue in Medical Diagnostics: Present Status and Future Promises. *Spectroscopy* **2012**, *27* (5–6), 463–496.
- (8) Derenne, A.; Gasper, R.; Goormaghtigh, E. The FTIR Spectrum of Prostate Cancer Cells Allows the Classification of Anticancer Drugs According to Their Mode of Action. *Analyst* **2011**, *136* (6), 1134–1141.
- (9) Delbeck, S.; Heise, H. M. FT-IR versus EC-QCL Spectroscopy for Biopharmaceutical Quality Assessment with Focus on Insulin—Total Protein Assay and Secondary Structure Analysis Using Attenuated Total Reflection. *Anal. Bioanal. Chem.* **2020**, *412* (19), 4647–4658.
- (10) Sala, A.; Spalding, K. E.; Ashton, K. M.; Board, R.; Butler, H. J.; Dawson, T. P.; Harris, D. A.; Hughes, C. S.; Jenkins, C. A.; Jenkinson, M. D.; Palmer, D. S.; Smith, B. R.; Thornton, C. A.; Baker, M. J. Rapid Analysis of Disease State in Liquid Human Serum Combining Infrared Spectroscopy and "Digital Drying. *J. Biophotonics* **2020**, *13* (9), No. e202000118.
- (11) Grenci, G.; Birarda, G.; Mitri, E.; Businaro, L.; Pacor, S.; Vaccari, L.; Tormen, M. Optimization of Microfluidic Systems for

- IRMS Long Term Measurement of Living Cells. *Microelectron. Eng.* **2012**, *98*, *698*–702.
- (12) Vaccari, L.; Birarda, G.; Businaro, L.; Pacor, S.; Grenci, G. Infrared Microspectroscopy of Live Cells in Microfluidic Devices (MD-IRMS): Toward a Powerful Label-Free Cell-Based Assay. *Anal. Chem.* **2012**, *84* (11), 4768–4775.
- (13) Chan, K. L. A.; Fale, P. L. V. Label-Free in Situ Quantification of Drug in Living Cells at Micromolar Levels Using Infrared Spectroscopy. *Anal. Chem.* **2014**, *86* (23), 11673–11679.
- (14) Fale, P. L.; Altharawi, A.; Chan, K. A. In Situ Fourier Transform Infrared Analysis of Live Cells' Response to Doxorubicin. *Biochim. Biophys. Acta, Mol. Cell Res.* **2015**, *1853* (10), 2640–2648.
- (15) Altharawi, A.; Rahman, K. M.; Chan, K. L. A. Towards Identifying the Mode of Action of Drugs Using Live-Cell FTIR Spectroscopy. *Analyst* **2019**, *144* (8), 2725–2735.
- (16) Aonuma, Y.; Kondo, Y.; Hirano-Iwata, A.; Nishikawa, A.; Shinohara, Y.; Iwata, H.; Kimura, Y.; Niwano, M. Label-Free and Real Time Monitoring of Adipocyte Differentiation by Surface Infrared Spectroscopy. Sens. Actuators, B 2013, 176, 1176–1182.
- (17) Andrew Chan, K. L.; Kazarian, S. G. Attenuated Total Reflection Fourier-Transform Infrared (ATR-FTIR) Imaging of Tissues and Live Cells. *Chem. Soc. Rev.* **2016**, *45* (7), 1850–1864.
- (18) Yamaguchi, R. T.; Hirano-Iwata, A.; Kimura, Y.; Niwano, M.; Miyamoto, K. I.; Isoda, H.; Miyazaki, H. In Situ Real-Time Monitoring of Apoptosis on Leukemia Cells by Surface Infrared Spectroscopy. *J. Appl. Phys.* **2009**, *105* (2), 024701.
- (19) Flower, K. R.; Khalifa, I.; Bassan, P.; Démoulin, D.; Jackson, E.; Lockyer, N. P.; McGown, A. T.; Miles, P.; Vaccari, L.; Gardner, P. Synchrotron FTIR Analysis of Drug Treated Ovarian A2780 Cells: An Ability to Differentiate Cell Response to Different Drugs? *Analyst* **2011**, *136* (3), 498–507.
- (20) Gough, K. M.; Tzadu, L.; Kastyak, M. Z.; Kuzyk, A. C.; Julian, R. L. Theoretical and Experimental Considerations for Interpretation of Amide I Bands in Tissue. *Vib. Spectrosc.* **2010**, *53* (1), 71–76.
- (21) Gazi, E.; Dwyer, J.; Lockyer, N. P.; Miyan, J.; Gardner, P.; Hart, C. A.; Brown, M. D.; Clarke, N. W. A Study of Cytokinetic and Motile Prostate Cancer Cells Using Synchrotron-Based FTIR Microspectroscopic Imaging. *Vib. Spectrosc.* **2005**, *38* (1–2), 193–201.
- (22) Spalding, K.; Bonnier, F.; Bruno, C.; Blasco, H.; Board, R.; Benz-de Bretagne, I.; Byrne, H. J.; Butler, H. J.; Chourpa, I.; Radhakrishnan, P.; Baker, M. J. Enabling Quantification of Protein Concentration in Human Serum Biopsies Using Attenuated Total Reflectance Fourier Transform Infrared (ATR-FTIR) Spectroscopy. *Vib. Spectrosc.* **2018**, *99*, 50–58.
- (23) Hughes, C.; Brown, M.; Clemens, G.; Henderson, A.; Monjardez, G.; Clarke, N. W.; Gardner, P. Assessing the Challenges of Fourier Transform Infrared Spectroscopic Analysis of Blood Serum. *J. Biophotonics* **2014**, *7* (3–4), 180–188.
- (24) Palano, G.; Jansson, M.; Backmark, A.; Martinsson, S.; Sabirsh, A.; Hultenby, K.; Åkerblad, P.; Granberg, K. L.; Jennback-en, K.; Müllers, E.; Hansson, E. M. A High-Content, in Vitro Cardiac Fibrosis Assay for High-Throughput, Phenotypic Identification of Compounds with Anti-Fibrotic Activity. *J. Mol. Cell. Cardiol.* **2020**, 142, 105–117.
- (25) Butler, H. J.; Brennan, P. M.; Cameron, J. M.; Finlayson, D.; Hegarty, M. G.; Jenkinson, M. D.; Palmer, D. S.; Smith, B. R.; Baker, M. J. Development of High-Throughput ATR-FTIR Technology for Rapid Triage of Brain Cancer. *Nat. Commun.* **2019**, *10*, 4501.
- (26) Schumacher, H.; Künzelmann, U.; Vasilev, B.; Eichhorn, K.-J.; Bartha, J. W. Applications of Microstructured Silicon Wafers as Internal Reflection Elements in Attenuated Total Reflection Fourier Transform Infrared Spectroscopy. *Appl. Spectrosc.* **2010**, *64* (9), 1022–1027.
- (27) Morhart, T. A.; Read, S. T.; Wells, G.; Jacobs, M.; Rosendahl, S. M.; Achenbach, S.; Burgess, I. J. Micromachined Multigroove Silicon ATR FT-IR Internal Re-flection Elements for Chemical Imaging of Microfluidic Devices. *Anal. Methods* **2019**, *11* (45), 5776–5783.
- (28) Kelp, G.; Arju, N.; Lee, A.; Esquivel, E.; Delgado, R.; Yu, Y.; Dutta-Gupta, S.; Sokolov, K.; Shvets, G. Application of Metasurface-

- Enhanced Infra-Red Spectroscopy to Distinguish between Normal and Cancerous Cell Types. *Analyst* **2019**, *144* (4), 1115–1127.
- (29) Kelp, G.; Li, J.; Lu, J.; DiNapoli, N.; Delgado, R.; Liu, C.; Fan, D.; Dutta-Gupta, S.; Shvets, G. Infrared Spectroscopy of Live Cells from a Flowing Solution Using Electrically-Biased Plasmonic Metasurfaces. *Lab Chip* **2020**, *20* (12), 2136–2153.
- (30) Huang, S. H.; Li, J.; Fan, Z.; Delgado, R.; Shvets, G. Monitoring the Effects of Chemical Stimuli on Live Cells with Metasurface-Enhanced Infrared Reflection Spectroscopy. *Lab Chip* **2021**, *21* (20), 3991–4004.
- (31) Huang, S. H.; Sartorello, G.; Shen, P. T.; Xu, C.; Elemento, O.; Shvets, G. Metasurface-Enhanced Infrared Spectroscopy in Multiwell Format for Real-Time Assaying of Live Cells. *Lab Chip* **2023**, 23, 2228–2240.
- (32) Shen, P. T.; Huang, S. H.; Huang, Z.; Wilson, J. J.; Shvets, G. Probing the Drug Dynamics of Chemotherapeutics Using Metasurface-Enhanced Infrared Reflection Spectroscopy of Live Cells. *Cells* **2022**, *11* (10), 1600.
- (33) Rodrigo, D.; Tittl, A.; Ait-Bouziad, N.; John-Herpin, A.; Limaj, O.; Kelly, C.; Yoo, D.; Wittenberg, N. J.; Oh, S. H.; Lashuel, H. A.; Altug, H. Resolving Molecule-Specific Information in Dynamic Lipid Membrane Processes with Multi-Resonant Infrared Metasurfaces. *Nat. Commun.* **2018**, *9* (1), 2160.
- (34) Lamb, H. On the Reflection and Transmission of Electric Waves by a Metallic Grating. *Proc. London Math. Soc.* **1897**, *s1*–29 (1), 523.
- (35) Derenne, A.; Claessens, T.; Conus, C.; Goormaghtigh, E. Infrared Spectroscopy of Membrane Lipids. In *Encyclopedia of Biophysics*; Springer, 2013; pp 1074–1081..
- (36) Barth, A. Infrared Spectroscopy of Proteins. *Biochim. Biophys. Acta, Bioenerg.* **2007**, *1767* (9), 1073–1101.
- (37) Poonprasartporn, A.; Chan, K. A. Live-Cell ATR-FTIR Spectroscopy as a Novel Bioanalytical Tool for Cell Glucose Metabolism Research. *Biochim. Biophys. Acta, Mol. Cell Res.* **2021**, 1868 (7), 119024.
- (38) Brooke, H.; Bronk, B. V.; McCutcheon, J. N.; Morgan, S. L.; Myrick, M. L. A Study of Electric Field Standing Waves on Reflection Microspectroscopy of Polystyrene Particles. *Appl. Spectrosc.* **2009**, *63* (11), 1293–1302.
- (39) Bassan, P.; Byrne, H. J.; Lee, J.; Bonnier, F.; Clarke, C.; Dumas, P.; Gazi, E.; Brown, M. D.; Clarke, N. W.; Gardner, P. Reflection Contributions to the Dispersion Artefact in FTIR Spectra of Single Biological Cells. *Analyst* **2009**, *134* (6), 1171–1175.
- (40) Filik, J.; Frogley, M. D.; Pijanka, J. K.; Wehbe, K.; Cinque, G. Electric Field Standing Wave Artefacts in FTIR Micro-Spectroscopy of Biological Materials. *Analyst* **2012**, *137* (4), 853–861.
- (41) Kitamura, R.; Pilon, L.; Jonasz, M. Optical Constants of Silica Glass from Extreme Ultraviolet to Far Infrared at near room Temperature. *Appl. Opt.* **2007**, *46* (33), 8118–8133.
- (42) Schwaighofer, A.; Akhgar, C. K.; Lendl, B. Broadband Laser-Based Mid-IR Spectroscopy for Analysis of Proteins and Monitoring of Enzyme Activity. *Spectrochim. Acta, Part A* **2021**, 253, 119563.
- (43) Grdadolnik, J.; Maréchal, Y. Bovine Serum Albumin Observed by Infrared Spectrometry. II. Hydration Mechanisms and Interaction Configurations of Embedded H(2)O Molecules. *Biopolymers* **2000**, *62* (1), 54–67.
- (44) Mittal, V.; Nedeljkovic, M.; Carpenter, L. G.; Khokhar, A. Z.; Chong, H. M. H.; Mashanovich, G. Z.; Bartlett, P. N.; Wilkinson, J. S. Waveguide Absorption Spectroscopy of Bovine Serum Albumin in the Mid-Infrared Fingerprint Region. ACS Sens. 2019, 4 (7), 1749–1753.
- (45) Haas, J.; Müller, A.; Sykora, L.; Mizaikoff, B. Analytical Performance of μ -Groove Silicon Attenuated Total Reflection Waveguides. *Analyst* **2019**, *144* (10), 3398–3404.
- (46) Kim, D. J.; Seol, J. K.; Lee, G.; Kim, G. S.; Lee, S. K. Cell Adhesion and Migration on Nanopatterned Substrates and Their Effects on Cell-Capture Yield. *Nanotechnology* **2012**, 23 (39), 395102. (47) Zeng, Y.; Wong, S. T.; Teo, S. K.; Leong, K. W.; Chiam, K. H.;

Yim, E. K. F. Human Mesenchymal Stem Cell Basal MembraneBend-

- ing on Gratings Is Dependent on Both Grating Width and Curvature. Sci. Rep. 2018, 8 (1), 6444.
- (48) Peer, E.; Artzy-Schnirman, A.; Gepstein, L.; Sivan, U. Hollow Nanoneedle Array and Its Utilization for Repeated Administration of Biomolecules to the Same Cells. *ACS Nano* **2012**, *6* (6), 4940–4946.
- (49) Caprettini, V.; Huang, J. A.; Moia, F.; Jacassi, A.; Gonano, C. A.; Maccaferri, N.; Capozza, R.; Dipalo, M.; De Angelis, F. Enhanced Raman Investigation of Cell Membrane and Intracellular Compounds by 3D Plasmonic Nanoelectrode Arrays. *Adv. Sci.* **2018**, *5*, 1800560.
- (50) Xie, C.; Lin, Z.; Hanson, L.; Cui, Y.; Cui, B. Intracellular Recording of Action Potentials by Nanopillar Electroporation. *Nat. Nanotechnol.* **2012**, *7* (3), 185–190.
- (51) Zhao, W.; Hanson, L.; Lou, H. Y.; Akamatsu, M.; Chowdary, P. D.; Santoro, F.; Marks, J. R.; Grassart, A.; Drubin, D. G.; Cui, Y.; Cui, B. Nanoscale Manipulation of Membrane Curvature for Probing Endocytosis in Live Cells. *Nat. Nanotechnol.* **2017**, *12* (8), 750–756.
- (52) Li, X.; Matino, L.; Zhang, W.; Klausen, L.; McGuire, A. F.; Lubrano, C.; Zhao, W.; Santoro, F.; Cui, B. A Nanostructure Platform for Live-Cell Manipulation of Membrane Curvature. *Nat. Protoc.* **2019**, *14* (6), 1772–1802.
- (53) Li, X.; Zhang, W.; Tsai, C. T.; Cui, B. Vertical Nanostructures for Probing Live Cells. In *Micro and Nano Systems for Biophysical Studies of Cells and Small Organisms*; Elsevier, 2021; Vol 3, pp 43–70..
- (54) Roy, A. R.; Zhang, W.; Jahed, Z.; Tsai, C. T.; Cui, B.; Moerner, W. E. Exploring Cell Surface-Nanopillar Interactions with 3D Super-Resolution Microscopy. ACS Nano 2022, 16 (1), 192–210.
- (55) Mettlen, M.; Danuser, G. Imaging and Modeling the Dynamics of Clathrin-Mediated Endocytosis. *Cold Spring Harbor Perspect. Biol.* **2014**, *6* (12), a017038.
- (56) Rennick, J. J.; Johnston, A. P. R.; Parton, R. G. Key Principles and Methods for Studying the Endocytosis of Biological and Nanoparticle Therapeutics. *Nat. Nanotechnol.* **2021**, *16*, 266–276.
- (57) McMahon, H. T.; Boucrot, E. Molecular Mechanism and Physiological Functions of Clathrin-Mediated Endocytosis. *Nat. Rev. Mol. Cell Biol.* **2011**, *12*, 517–533.
- (58) Berthing, T.; Bonde, S.; Sørensen, C. B.; Utko, P.; Nygård, J.; Martinez, K. L. Intact Mammalian Cell Function on Semicon-ductor Nanowire Arrays: New Perspectives for Cell-Based Biosensing. *Small* **2011**, *7* (5), 640–647.
- (59) Oakley, C.; Jaeger, N. A. F.; Brunette, D. M. Sensitivity of Fibroblasts and Their Cytoskeletons to Substratum Topographies: Topographic Guidance and Topographic Compensation by Micromachined Grooves of Different Dimensions. *Exp. Cell Res.* **1997**, 234 (2), 413–424.
- (60) Teixeira, A. I.; Abrams, G. A.; Bertics, P. J.; Murphy, C. J.; Nealey, P. F. Epithelial Contact Guidance on Well-Defined Microand Nanostructured Substrates. *J. Cell Sci.* **2003**, *116* (10), 1881–1892.
- (61) Den Braber, E. T.; de Ruijter, J. E.; Smits, H. T. J.; Ginsel, L. A.; von Recum, A. F.; Jansen, J. A. Effect of Parallel Surface Microgrooves and Surface Energy on Cell Growth. *J. Biomed. Mater. Res.* **1995**, 29 (4), 511–518.
- (62) Den Braber, E. T.; De Ruijter, J. E.; Smits, H. T. J.; Ginsel, L. A.; Von Recum, A. F.; Jansen, J. A. Quantitative Analysis of Cell Proliferation and Orientation on Substrata with Uniform Parallel Surface Micro-Grooves. *Biomaterials* 1996, 17 (11), 1093–1099.
- (63) Meyle, J.; Gultig, K.; Brich, M.; Ham-merle, H.; Nisch, W. Contact Guidance of Fibroblasts on Biomaterial Surfaces. *J. Mater. Sci.: Mater. Med.* **1994**, *5*, 463–466.
- (64) Britland, S.; Morgan, H.; Wojiak-Stodart, B.; Riehle, M.; Curtis, A.; Wilkinson, C. Synergistic and Hierarchical Adhesive and Topographic Guidance of BHK Cells. *Exp. Cell Res.* **1996**, 228, 313–325.
- (65) Meyle, J.; Gültig, K.; Nisch, W. Variation in Contact Guidance by Human Cells on a Microstructured Surface. *J. Biomed. Mater. Res.* **1995**, 29 (1), 81–88.
- (66) Higgins, S. G.; Becce, M.; Belessiotis-Richards, A.; Seong, H.; Sero, J. E.; Stevens, M. M. High-Aspect-Ratio Nanostructured

- Surfaces as Biological Metamaterials. Adv. Mater. 2020, 32 (9), 1903862.
- (67) Nomura, S.; Kojima, H.; Ohyabu, Y.; Kuwabara, K.; Miyauchi, A.; Uemura, T. Nanopillar Sheets as a New Type of Cell Culture Dish: Detailed Study of HeLa Cells Cultured on Nanopillar Sheets. *J. Artif. Organs* **2006**, *9* (2), 90–96.
- (68) Liu, W. F.; Chen, C. S. Cellular and Multicellular Form and Function. Adv. Drug Delivery Rev. 2007, 59 (13), 1319-1328.
- (69) Wang, S.; Wang, H.; Jiao, J.; Chen, K. J.; Owens, G. E.; Kamei, K. I.; Sun, J.; Sherman, D. J.; Behrenbruch, C. P.; Wu, H.; Tseng, H. R. Three-Dimensional Nanostructured Substrates toward Efficient Capture of Circulating Tumor Cells. *Angew. Chem., Int. Ed.* **2009**, 48 (47), 8970–8973.
- (70) Martin, F. L.; Kelly, J. G.; Llabjani, V.; Martin-Hirsch, P. L.; Patel, I. I.; Trevisan, J.; Fullwood, N. J.; Walsh, M. J. Distinguishing Cell Types or Populations Based on the Computational Analysis of Their Infrared Spectra. *Nat. Protoc.* **2010**, *5* (11), 1748–1760.
- (71) Mittal, S.; Yeh, K.; Leslie, L. S.; Kenkel, S.; Kajdacsy-Balla, A.; Bhargava, R. Simultaneous Cancer and Tumor Microenvironment Subtyping Using Confocal Infrared Microscopy for All-Digital Molecular Histopathology. *Proc. Natl. Acad. Sci. U.S.A.* **2018**, *115* (25), No. E5651.
- (72) Hanson, L.; Zhao, W.; Lou, H. Y.; Lin, Z. C.; Lee, S. W.; Chowdary, P.; Cui, Y.; Cui, B. Vertical Nanopillars for in Situ Probing of Nuclear Mechanics in Adherent Cells. *Nat. Nanotechnol.* **2015**, *10* (6), 554–562.